

Date of publication xxxx 00, 0000, date of current version xxxx 00, 0000.

Digital Object Identifier 10.1109/ACCESS.2017.Doi Number

# Current-source Single-phase Module Integrated Inverters for PV Grid-connected Applications

Ahmed Darwish<sup>1</sup>, Saud Alotaibi<sup>1</sup>, and Mohamed A. Elgenedy<sup>2,3</sup>, Senior Member, IEEE

<sup>1</sup>Engineering Department, Lancaster University, Lancaster, LA1 4WY, United Kingdom.

<sup>2</sup>Electrical Engineering Department, University of Strathclyde, 6 Richmond St, Glasgow G1 1XQ

<sup>3</sup>Electrical Power Engineering, Alexandria University, Alexandria, Egypt

\*Corresponding author: Ahmed Darwish (e-mail: a.badawy@lancaster.ac.uk).

**ABSTRACT** This paper presents a modular grid-connected single-phase system based on series-connected current-source module integrated converters (MICs). The modular configuration improves the reliability, redundancy and scalability of photovoltaic (PV) distributed generators. In this system, each PV panel is connected to a dc/ac inverter to permit individual Maximum Power Point Tracking (MPPT) operation for each panel. Thus, the harvested power from the PV system will increase significantly. There are four different inverter topologies suitable to be used as MICs with different performances in terms of filtering elements size, power losses, efficiency, output voltage range, and high frequency transformers' size. For the MPPT control, the oscillating even order harmonic components should be eliminated from the inverter's input side otherwise the maximum power cannot be extracted. The proposed modulation scheme in this paper will ease the control of inverter's input and output sides. Therefore, the 2<sup>nd</sup> order harmonic in the input current can be eliminated without adding new active semiconductor switches. A repetitive controller coupled with proportional-resonant controllers are employed to achieve accurate tracking for grid side as well as input side currents. Comparisons and performance evaluations for the proposed MICs are presented and validated with 1 kVA prototype controlled by TMS320F29335 DSP.

**INDEX TERMS** Photovoltaic generation, , Series-connected, power decoupling, Cuk converter, Sepic converter.

## I. INTRODUCTION

The remarkable development in the installed capacity of distributed generators (DGs) increases the international aspiration for improving the performance of power inverters employed in renewable energy systems (RESs) such as photovoltaic (PV) systems [1]. The employed inverters are required to have small size, light weight and low power losses. The inverter's power losses are generated from several sources including conduction, switching losses in the semiconductor devices, and equivalent series resistance (ESR) in the inductors and capacitors. Another implicit source of PV system's power losses is when the PV panel is not able to produce its maximum power because of drawing time-variant currents by the employed inverter. In this case, the maximum power point tracking (MPPT) controller fails to operate the system at the peak of the P-V curve, see Fig. 1a. As reviewed in [2]–[4], the PV systems can be classified into three main categories: string inverter, centralised inverter, and ac module. Traditionally, the centralised and the string inverter systems are preferred for their power density, reduced cost and power losses. Thus, they dominated the

commercial market. In the centralised inverter systems, PV modules are connected in series to boost the dc voltage bus. Then, a centralised inverter generates the necessary ac voltages and currents to be fed to the residential ac loads or to be injected into the local grid. Thus, the PV panels share the same dc current and the MPPT operation becomes complicated. Although the centralised inverter systems reduce the power losses inside the power converters, the harvested energy is reduced because of the MPPT may not be achieved in all circumstances. In addition, the central inverter transfers the total power and therefore the system's scalability is restricted [3]. In ac module system, the PV panels are connected to micro-inverters which boosts the low dc voltage from a single panel to higher ac voltage at the grid frequency [4]. Because each PV panel is connected to a micro-inverter, the output current of each panel can be independently controlled and therefore a better MPPT performance can be achieved. Because it is simple to assemble, it can be used by users without professional knowledge and skills as "plug-and-play" systems [5]. On the downside, the micro-inverter is required to provide high

boosting ratio to match the PV panels' voltages to the grid's ac voltage level and hence the semiconductor losses are increased and the power density may be reduced [5]. Due to the increased voltage and current stresses, the micro-inverter's reliability will be affected. Also, without central high voltage dc-bus the micro-inverter is required to decouple the instantaneous pulsating 2<sup>nd</sup> order harmonic energy components generated in single-phase systems otherwise the MPPT will not be achieved [6]. As a compromise between centralised, string and ac module structures, the series-connected modular structure can improve the performance of the grid-tied PV system significantly [7]. As shown in Fig. 1b, each module in this system is connected to a single PV panel while the output sides of the symmetrical modules are connected in series to match the output voltage at the point of common coupling (PCC) to the grid voltage. Thus, the voltage and current stresses in the module inverters are shared between the inverters' devices and hence the reliability increases, and the power losses decreases. Moreover, the modular structure of the series-connected system provides a degree of redundancy and scalability.

To draw constant currents from the PV panels and extract the maximum power, two current components in the input side current should be minimised. The first is the high frequency (HF) current ripple which can be eliminated by an input filtering such as capacitors or inductors [8]. In most of cases, a bulky electrolytic capacitor is employed as an input filter and therefore the power density is reduced. Moreover, the lifetime of this capacitor is halved for 10 °C increase in the temperature and hence, the inverter's reliability is limited [8]. With current-sourced inverters, the HF current ripple is eliminated with an input inductor and, if necessary, small plastic capacitors [9]. The second current component to be eliminated is the 2<sup>nd</sup> order harmonic current which is generated from the operation of single-phase inverters. This component should be decoupled to enable the MPPT controller to settle at the peak of the P-V curve and harvest the maximum available power in the solar source.

To eliminate the leakage currents flowing between the PV neutral point and the ac network ground which create hazards, and affect the operation and lifetime, the selected modules are isolated with small-size HF transformer cores [10]-[12].

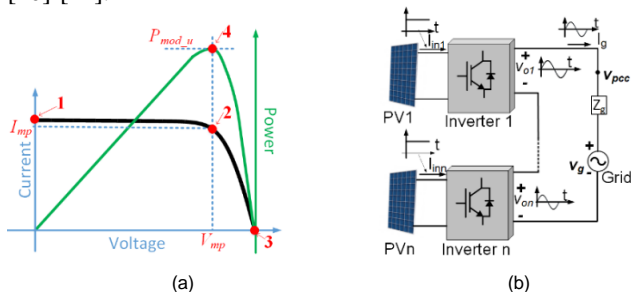


FIGURE 1. Grid-connected PV system: (a) I-V and P-V curves and (b) Modular configuration

The transformer cores' sizes can be reduced by increasing the switching frequency of the semiconductor devices in the inverter. Moreover, the isolating HF transformers provide voltage boosting and reduce Electro-Magnetic Interference (EMI). Examining the different structures of power electronic converters, four buck-boost converters can be found with the features stated earlier [12], [13]. These converters are demonstrated in Fig. 2 and will be labelled in this paper as C5 (Cuk), F5, G5 (SEPIC), and P5. The single-phase descendants from these converters are generated and shown in Fig. 3.

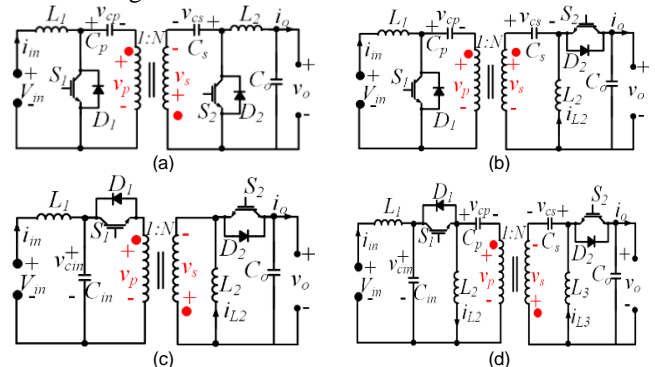


FIGURE 2. isolated converters (a) C5 (Cuk), (b) F5, (c) G5 (Sepic), (d) P5

These four inverter modules can be employed in the modular PV system in Fig. 1b provided that the input power is decoupled from output. This paper proposes modified modulation schemes for the single-phase inverters in Fig. 3 where the output bridge switches are operated independently with respect to the input side to provide an additional degree of freedom. In this way, both input and output sides' currents can be controlled together and the even harmonics in the input currents will be eliminated and hence the MPPT controller will be able to maximise the output power of the system. Because the proposed converters and their descendants have two or more right-half-plane (RHP) zeros, the classical controllers will not be able to give the required gain at 50 Hz (i.e to reduce the sensitivity function  $S(s)$  gain) and provide the required stability margins in the same time. Therefore, this paper presents a control scheme based on Feed-Forward Repetitive Control (RC) with a Proportional-resonant (PR) controller to ensure that the reference signals can be tracked and the stability conditions will be satisfied. The proposed controller can provide good disturbance rejections at the multiples of the controller periodic signals. The PR controllers are responsible for tracking the reference signals with zero steady-state errors.

The rest of this paper is organised as follows: Section. II presents the operation's concept of the inverters. Section III presents the modified modulation techniques of the inverters. The generic operation of the modular system is explained in and Section IV. Section V presents the RC control scheme used to operate the system. Section VI presents the experimental results of the MIC PV system using the four inverters. The parameter's selection process as well as

comparisons between the different modules are presented in section VII.

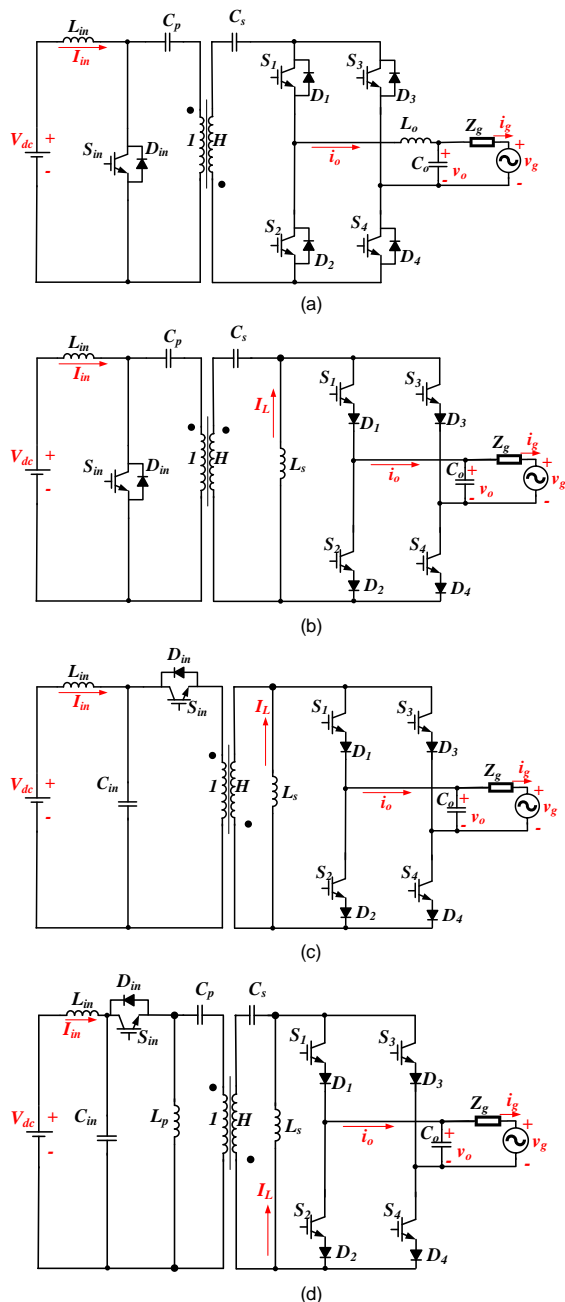


FIGURE 3. Single-phase inverter modules: (a) Cuk, (b) Sepic, (c) F5 and (d) P5

## II. INVERTER MODULES

Some single-phase descendants of the Cuk and Sepic converters have been published in [14]-[17]. In all these single-phase inverters, the output switches are operating in a complementary manner with the input side switch. Consequently, only the input or the output sides' currents can be controlled. In these inverters, the output current is controlled to inject the required power into the local grid while the input side current is left uncontrolled. The published single-phase inverters can be categorized into

three main types. The first is the differential inverter as presented in [14] and [17], see Fig. 4a.

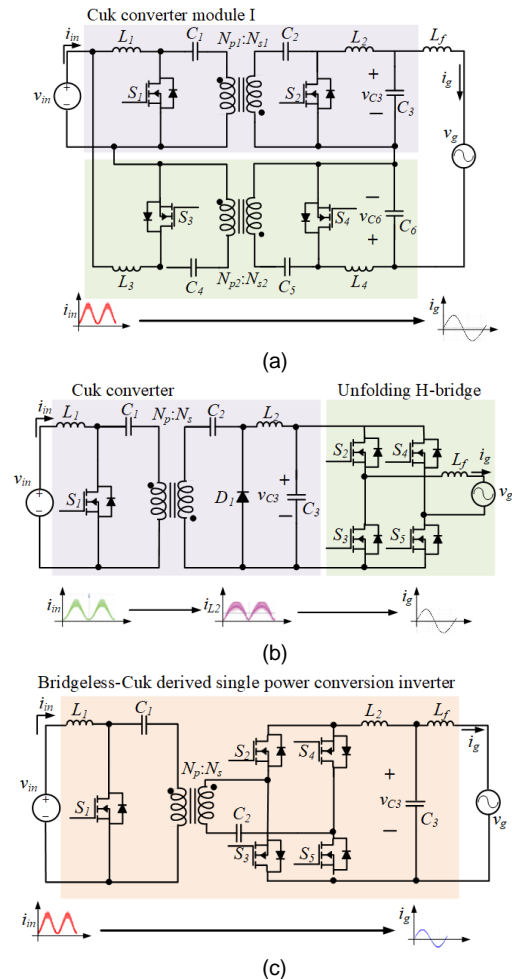


FIGURE 4. Cuk-based inverters: (a) Differential configuration in [14] and [17] (b) Unfolding-type in [15] and (c) Bridgeless type in [16]

In this configuration, two two-switch two-diodes Cuk converters are connected differentially across the ac load. Each converter, by controlling its input side switch, produces one half-cycle of the output voltage and current. The unfolding-type Cuk inverter has been proposed in [15], see Fig. 4b. In this type, the rectified voltage is generated across  $C_3$  with controlling the input switch  $S_1$  and then this voltage is directed to the output load using the bridge switches  $S_2 \rightarrow S_5$ . This means that the controlling device is  $S_1$  while the switches ( $S_2$  and  $S_5$ ) are ON for the positive half-cycle of the generated 50/60 Hz voltage while ( $S_3$  and  $S_4$ ) are ON for the negative half-cycle. In the bridgeless Cuk inverter proposed in [16], see Fig. 4c, the bridge has been moved before the output stage to improve the efficiency. With the same modulation concept, the input switch  $S_1$  is responsible for shaping the output voltage while  $S_2 \rightarrow S_5$  are only directors for the positive and negative parts of the ac waveforms. Because only one switch is responsible for generating the output voltage/current in the abovementioned inverters, it is only

possible to control either the output or the input sides. Because of the oscillating power nature in ac single-phase operation, the input current will be composed of a dc plus a 2nd order harmonic components if only the output side is controlled. It is can be deduced from curves in Fig. 1a and the input currents of the inverters in Fig. 4 that the operational points with the time-variant input currents will be oscillating between the points 2 and 3 of the I-V curve. This causes the power to be oscillating between points 4 and 3 which prevents achieving the PV maximum power and increases the temperature of the PV module, and decrease its lifetime [10]. The next section presents the modified modulation scheme for the proposed inverters in order to fix this problem and eliminate the even harmonics from the input side currents.

### III. MODULATION SCHEMES

Without loss of generality, the analysis and principle of operation will be explained for the Cuk-based module, in Fig. 3a, and the operation of the other candidates can then be deduced similarly. The main difference between these inverters is in the element that stores the oscillating energy. A discussion regarding to this issue will be considered later in this paper. To operate the Cuk module in continuous current mode (CCM), the input and output inductors ( $L_{in}$  and  $L_{out}$ ) will be assumed large enough. The module has one switch at the input side  $S_{in}$  and four switches at the output bridge  $S_1 \rightarrow S_4$ .

#### A. MODES OF OPERATION

There are three operating modes for this inverter from the perspective of the middle capacitors  $C_p$  and  $C_s$ , charging mode M1, discharging mode M2, and charging mode M3. If  $i_g$  is positive, the operation can be described as:

- During M1 ( $0 \leq t < t_{off}$ ),  $S_{in}$  is turned OFF while one of the switches  $S_1$  or  $S_4$  is switched ON. The input current  $i_{in}$  decreases and flows through  $C_p$  which stores energy, see Fig. 5a and Fig.6. Meanwhile, the output current  $i_o$  is flowing through  $D_2$ ,  $S_4$ , (or  $D_3$  and  $S_1$ ). When the grid current  $i_g$  reverses direction in the negative half-cycle, the output current passes through  $S_2$  and  $D_4$  (or  $D_1$  and  $S_3$ ) while the input side remains the same.
- During M2 ( $t_{off} \leq t < t_{off} + t_1$ ),  $S_{in}$  is turned ON leading  $i_{in}$  to increase. As in Fig. 5b,  $i_o$  flows through  $S_1$  and  $S_4$ . As  $C_p$  and  $C_s$  discharge during this mode, their energy transfers to  $L_o$  and the output current increases. During the negative cycle of  $i_g$ , the output current flows through  $S_2$  and  $S_3$  while the input side remains the same.
- During M3 ( $t_{off} + t_1 \leq t < t_s$ ),  $S_{in}$  is turned ON and the input current is still increasing. The output current flows through freewheeling diodes  $D_2$  and  $D_3$  (or  $D_1$  and  $D_4$  if it is in the negative half cycle).  $C_p$  and  $C_s$  are charging leading  $i_o$  to decrease. This mode, where the input current is increasing while the output current is decreasing, does not exist in the Cuk converter and its inverter descendants

described presented in [14]-[15]. Because it adds an additional degree of freedom, this mode enables the decoupling of the input and output currents behaviors and therefore it helps in controlling both input and output currents. The theoretical waveforms of the proposed inverter are shown in Fig. 6.

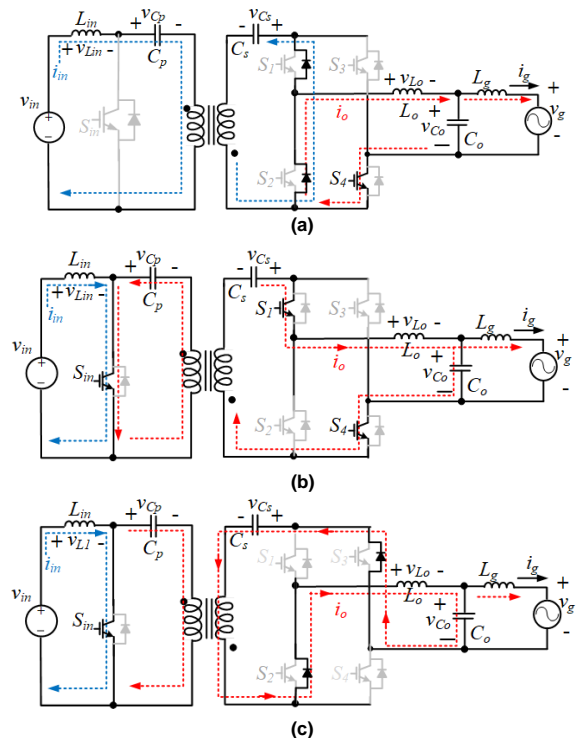


FIGURE 5. Operating modes of the Cuk inverter. (a) M1, (b) M2 and (c) M3

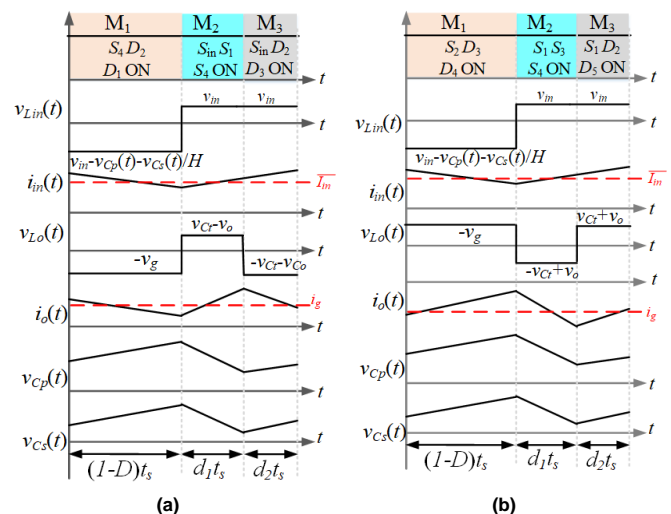


FIGURE 6. Theoretical waveforms of the Cuk inverter. (a) positive half cycle and (b) negative half cycle

#### B. AVERAGE MODEL OF THE INVERTER

Assuming that  $d_1$  and  $d_2$  are the duty cycle ratios of modes M2 and M3 respectively, they can be expressed as:

$$d_1 = \frac{t_1}{t_s}, \quad d_2 = \frac{t_2}{t_s} \quad \text{and} \quad D = d_1 + d_2 \quad (1)$$

$$\dot{x}(t) = \begin{bmatrix} 0 & \frac{D-1}{HL_m} & 0 & 0 & 0 \\ \frac{1-D}{HC_{eq}} & 0 & \frac{d_2-d_1}{HC_{eq}} & 0 & 0 \\ 0 & \frac{d_1-d_2}{L_o} & 0 & \frac{-1}{L_o} & 0 \\ 0 & 0 & \frac{1}{C_o} & 0 & \frac{-1}{C_o} \\ 0 & 0 & 0 & \frac{1}{L_g} & 0 \end{bmatrix} x(t) \quad (2)$$

$$+ \begin{bmatrix} \frac{1}{L_m} & 0 \\ 0 & 0 \\ 0 & 0 \\ 0 & 0 \\ 0 & \frac{-1}{L_g} \end{bmatrix} \begin{bmatrix} v_{in} \\ v_g \end{bmatrix}$$

Using the average modelling method in [9], [12], the Cuk-based module is averaged along the switching cycle  $t_s$  and the average model as in (2). where the state vector  $x(t) = [i_{in}(t) \quad v_{Ct}(t) \quad i_o(t) \quad v_o(t) \quad i_g(t)]$  and  $y(t) = i_g(t)$  is the grid current. The state  $v_{Ct}(t)$  is  $Hv_{Cp}(t) + v_{Cs}(t)$ ,  $H$  is the turns ratio ( $N_s/N_p$ ),  $C_t$  is  $C_p C_s / (C_p + H^2 C_s)$ ,  $d_1(t)$  is the duty cycle ratio of  $M_2$ ,  $d_2(t)$  is the duty cycle ratio of  $M_3$  while  $D(t)$  is the duty cycle ratio of switch  $S_{in}$ .

The grid voltage and current can be expressed as:

$$v_g = V_g \sin(\omega t) \quad (3a)$$

$$i_g = I_g \sin(\omega t - \gamma) \quad (3b)$$

Then, the instantaneous power injected to the grid ( $P_{grid}$ ) can be calculated from:

$$P_{grid}(t) = v_g(t) \cdot i_g(t) \quad (4a)$$

$$P_{grid}(t) = P_{dc} + P_{ac}(t) \quad (4b)$$

$$P_{dc} = \frac{V_g I_g \cos \gamma}{2} \quad (4c)$$

$$P_{ac} = \frac{V_g I_g}{2} \sin(2\omega t - \gamma - \frac{\pi}{2}) \quad (4d)$$

From (4d), the oscillating part of the inverter's power can be obtained from the known grid voltage and current ( $V_g$  and  $I_g$ ). As stated earlier, the additional mode of operation will add a new control parameter  $d_2$  which will allow for controlling the capacitors voltages  $v_{Ct}$ . This voltage can be controlled to generate the oscillating power component instead of supplying it from the input side as:

$$P_{ac}(t) + C_t v_{Ct}(t) \frac{dv_{Ct}(t)}{dt} = 0 \quad (5)$$

$$C_t v_{Ct}(t) \frac{dv_{Ct}(t)}{dt} = -P_{ac}(t) = \frac{V_g I_g \cos(2\omega t - \gamma)}{2} \quad (6)$$

It is shown that  $P_{ac}$  is composed of a 2<sup>nd</sup> order ac components, hence the desired capacitor voltage  $v_{Ct}$  can be assumed as:

$$v_{Ct}(t) = V_{Cdc} + V_{Cac} \sin(2\omega t + \phi) \quad (7)$$

Solving (6) and (7) yields:

$$\phi = \tan^{-1} \left( \frac{\omega L_o I_g \cos 2\gamma - V_g \sin 2\gamma}{V_g \cos 2\gamma + \omega L_g I_g \sin 2\gamma} \right) \quad (8)$$

$$V_{Cac} = \frac{V_g I_g \cos 2\gamma + \omega L_o I_g^2 \cos 2\gamma}{4\omega C_t V_{Cdc} \cos \phi} \quad (9)$$

Consequently, the oscillating component of the inverter's power can be eliminated from the input side by controlling the capacitors voltage  $v_{Ct}$  as in (7), (8) and (9). The required duty cycle ratios for that can be calculated from the state-space representation in (2). The first row of this representation can be written separately as:

$$\frac{di_{in}(t)}{dt} = \frac{D(t)-1}{HL_m} v_{Ct}(t) + \frac{1}{L_m} V_{in} \quad (10)$$

It is desired to keep the input current constant with time and therefore (10) can be re-written as:

$$0 = \frac{D(t)-1}{HL_m} v_{Ct}(t) + \frac{1}{L_m} V_{in} \quad (11)$$

$$D(t) = \frac{v_{Ct}(t) - H V_{in}}{v_{Ct}(t)}$$

In the same way, the third row of the state-space model is written as:

$$\frac{di_o(t)}{dt} = \frac{1-D(t)}{L_o} v_{Ct}(t) - \frac{d_2(t)-d_1(t)}{L_o} v_o(t) \quad (12)$$

Arranging (12), the duty cycle ratios can be found from:

$$d_1(t) = \frac{L_o \frac{di_o(t)}{dt} + v_o(t) - d_1(t)}{2v_{Ct}(t)} + \frac{D(t)}{2} \quad (13a)$$

$$d_2(t) = D(t) - d_1(t) \quad (13b)$$

The duty cycle ratios can be calculated from (13) assuming that  $i_o \approx i_g$  and  $v_o \approx v_g$ . These duty cycle ratios are compared with carrier signals at the switching frequency  $f_s = 1/t_s$  and used to operate the inverter's switches. Thus, the 2<sup>nd</sup> order component can be eliminated from the input side. With the duty-cycle ratios  $d_1$  and  $d_2$ , the inverter will be able to generate the required output sinusoidal current with keeping the input current constant with time which is necessary for MPPT operation. The calculations errors due to the parameters' mismatches, operational variations or external disturbances will be corrected by the closed-loop controller which will be presented later in this paper.

#### IV. MODULAR SYSTEM

The MIC based system is shown in Fig. 1b where the output voltages of the series  $n$  modules ( $v_{o1}$  to  $v_{on}$ ) are added together to generate the required total voltage,  $v_{PCC}$ , at the point of common coupling (PCC). The four candidates

shown in Fig. 3 can be used as inverter module with different advantages and disadvantages. The input PV modules can be connected separately to each inverter module (as shown in Fig. 1b) in case of low modules' currents while several modules can be connected to one PV array if the PV arrays' currents are high enough. If the input current of the inverter modules (output of the PV modules) is left uncontrolled, the operating point will be oscillating between points 3 and 4 in the power curve shown in Fig. 1a. So, the extracted power will be limited to almost have the available power from the PV module.

### A. Normal conditions

The grid current  $i_g$  flows through each modules' ac sides and determines the active and reactive power flow. Fig. 7 shows the phasor diagram and illustrate the system's currents and voltages with respect to the grid voltage  $v_g$ .

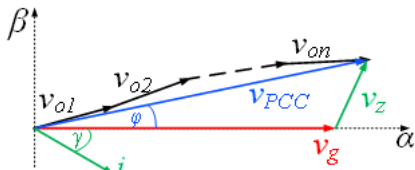


FIGURE 7. Phasor diagram of the modular converter in Fig. 1b

The inverters' voltages can be expressed as:

$$v_{o_j} = V_{o_j} \sin(\omega t + \theta_j) \quad (14)$$

$$\begin{aligned} v_{PCC} &= V_{o_1} \sin(\omega t + \theta_1) + V_{o_2} \sin(\omega t + \theta_2) + \dots + V_{o_n} \sin(\omega t + \theta_n) \\ &= \sum_{i=1}^n v_{o_j} = v_g + i_g Z_g \end{aligned} \quad (15)$$

where  $\theta_j$  is the module voltage phase angle,  $\gamma$  is the grid power factor angle, and  $Z_g$  is the grid impedance. In normal operation, the modules' output voltages have the same magnitude and phase angle as:

$$V_{o_1} = V_{o_2} = \dots = V_{o_n} \quad (16)$$

$$\theta_1 = \theta_2 = \dots = \theta_n \quad (17)$$

Starting from the normal conditions, the active power is evenly shared between the modules, the grid current is expressed as:

$$i_g(t) = \frac{n[V_o \sin(\omega t + \theta)] - V_g \sin(\omega t)}{Z_g} = I_m \sin(\omega t - \gamma) \quad (18)$$

If the cables losses are neglected, the total output power in normal conditions is calculated from:

$$P_{total} = \frac{nV_o I_g \cos(\theta - \gamma)}{2} \approx \frac{V_g I_g \cos(\gamma)}{2} \quad (19)$$

The power of each module is calculated from:

$$P_{mod_u} = V_{in} I_{in} = \frac{V_o I_g \cos(\theta - \gamma)}{2} \approx \frac{V_g I_g \cos(\theta - \gamma)}{2n} \quad (20)$$

If the desired operating point is known from the MPPT calculations at the optimum points ( $V_{in}$ ,  $I_{in}$ , and  $P_{mod_u}$ ), the reference grid current  $i_g$  can be obtained from (18), (19) and (20).

### B. Partial shading conditions

Fig. 8 shows the I-V and P-V characteristics during shading conditions where the shaded PV module is expected to reduce its maximum power point. Although the characteristics of the PV modules vary with their type and connection, the P-V curve will always have reduced peak value in shading conditions. Thus, the optimum points of the shaded modules move to ( $V_{in\_sh}$ ,  $I_{in\_sh}$ , and  $P_{mod\_sh}$ ) so the grid current should be changed to another value in order to extract the maximum available power from the shaded and unshaded PV modules.

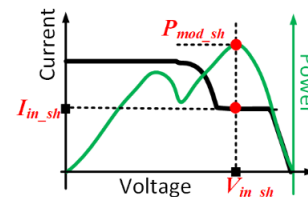


FIGURE 8. I-V and P-V characteristics of shaded PV arrays

To explain that, assume that  $k$  modules are shaded while other  $(n-k)$  modules are unshaded. The new grid current  $i_g'(t)$  can be expressed as:

$$\begin{aligned} i_g'(t) &= \frac{[kV_{o\_sh} \sin(\omega t + \theta_{sh}) + (n-k)V_o \sin(\omega t + \theta) - V_g \sin(\omega t)]}{Z_g} \\ &= I_g' \sin(\omega t - \gamma) \end{aligned} \quad (21)$$

where  $V_{o\_sh}$  and  $\theta_{sh}$  are the amplitude and the phase shift angle of the shaded modules' output voltages respectively while  $I_g'$  is the amplitude of the new grid current. The power of the shaded modules is calculated from:

$$P_{mod\_sh} = V_{in\_sh} I_{in\_sh} \approx \frac{V_{o\_sh} I_g' \cos(\theta_{sh} - \gamma)}{2} \quad (22)$$

The total power harvested from the system becomes:

$$P'_{total} = kV_{in\_sh} I_{in\_sh} + (n-k)V_{in} I_{in} \quad (23)$$

The power injected into the grid can be expressed as:

$$\begin{aligned} P'_{total} &= \frac{(n-k)V_o I_g' \cos(\theta - \gamma) + kV_{o\_sh} I_g' \cos(\theta_{sh} - \gamma)}{2} \\ &\approx \frac{V_g I_g' \cos(\gamma)}{2} \end{aligned} \quad (24)$$

To extract the maximum available power from the shaded and unshaded PV modules, the new reference value is set to  $I_g^*$  which can be obtained from solving (22), (23) and (24)

### V. CLOSED-LOOP CONTROL

The two RHP zeros in the Cuk inverter's transfer function complicate the control design. The RC-based control schemes learn the behaviour of the system with many repetition samples and use this information to reduce the system error and improve the tracking error in the next trial [18]-[20]. So, it can improve tracking accuracy with several repetitions [19]. The controller in Fig. 9 is composed of three

control loops with different tasks and this will be explained in the following subsections.

### A. OUTPUT PR CONTROLLER

A PR controller tuned at the grid angular frequency  $\omega$  is able to provide high gain at this frequency. The PR controller's transfer function in the continuous s-domain is:

$$G_{PR}(s) = k_p + \frac{k_r s}{s^2 + \omega^2} \quad (25)$$

where  $k_p$  and  $k_r$  are the proportional and resonant gains of the controller respectively. The transfer function in (25) can be discretised using Tustin method as:

$$G_{PR}(z) = k_p + \frac{2k_r t_s (1-z^{-2})}{4 + (\omega t_s)^2 + 2[(\omega t_s)^2 - 4]z^{-1} + [(\omega t_s)^2 + 4]z^{-2}} \quad (26)$$

As shown in the proposed controller in Fig. 9, the reference grid current  $I_g^*(z)$  is compared with the actual measured value of the grid current to give the errors signal  $E(z)$  which is fed to the PR controller. Then, the output of the PR controller is used as the duty cycle ratio input to the inverter module. To obtain the transfer function of the Cuk inverter  $G_{inv}(z)$ , the state space representation of the inverter is linearized as in [18] to obtain the small-signal model as in (27) where the superscript ' $\sim$ ' refers to the incremental variation of a state while the subscript ' $e$ ' stands for the equilibrium point of a state.

$$\dot{\tilde{x}}(t) = \begin{bmatrix} 0 & \frac{D_e - 1}{HL_{in}} & 0 & 0 & 0 \\ \frac{1-D_e}{HC_{eq}} & 0 & \frac{d_{2e} - d_{1e}}{HC_{eq}} & 0 & 0 \\ 0 & \frac{d_{1e} - d_{2e}}{L_o} & 0 & \frac{-1}{L_o} & 0 \\ 0 & 0 & \frac{1}{C_o} & 0 & \frac{-1}{C_o} \\ 0 & 0 & 0 & \frac{1}{L_g} & 0 \end{bmatrix} \tilde{x}(t) \quad (27)$$

$$+ \begin{bmatrix} \frac{V_{cte}}{HL_{in}} & \frac{V_{cte}}{HL_{in}} \\ \frac{-(I_{ine} + I_{ge})}{HC_{eq}} & \frac{(I_{ge} - I_{ine})}{HC_{eq}} \\ \frac{V_{cte}}{L_o} & \frac{-V_{cte}}{L_o} \\ 0 & 0 \\ 0 & 0 \end{bmatrix} \begin{bmatrix} \tilde{d}_1 \\ \tilde{d}_2 \end{bmatrix}$$

$$\tilde{y} = [0 \ 0 \ 0 \ 0 \ 1] \tilde{x}(t)$$

Based on the small signal model in (27), the s-domain transfer function between the control input  $d_i$  to the output  $i_g$  can be deduced as:

$$G_{inv}(s) = \frac{\tilde{i}_g(s)}{\tilde{d}_1(s)} = \frac{a_3 s^3 + a_2 s^2 + a_1 s + a_0}{b_5 s^5 + b_4 s^4 + b_3 s^3 + b_2 s^2 + b_1 s + b_0} \quad (28)$$

where the parameters  $a_i$  for  $i=1,2,3$  and  $b_j$  for  $j=1,\dots,5$  are omitted for brevity. To design the controller in discrete-time domain, the transfer function is obtained using Tustin method and arranged as:

$$G_{inv}(z) = \frac{\tilde{i}_g(z)}{\tilde{d}_1(z)} = \frac{m_5 z^5 + m_4 z^4 + m_3 z^3 + m_2 z^2 + m_1 z + m_0}{n_5 z^5 + n_4 z^4 + n_3 z^3 + n_2 z^2 + n_1 z + n_0} \quad (29)$$

Without the RC controller, the closed-loop transfer  $T(z)$  to control the output current  $i_g$  can be expressed as:

$$T(z) = \frac{\tilde{i}_g(z)}{I_g^*(z)} = \frac{G_{PR}(z)G_{inv}(z)}{1 + G_{PR}(z)G_{inv}(z)} \quad (30)$$

### B. FEED-FORWARD RC CONTROLLER

The feed-forward RC controller is shown in Fig. 9. The internal model principle (IMP) states that a closed-loop controller is able to eliminate the steady state error of a system if the sampling frequency of the controller is a multiple of the periodic signal which is desired to be controlled [19]. The required integral action can be modelled as unit delays. The ratio ( $N$ ) of the sampling frequency ( $f_s$ ) and the controlled signal's frequency ( $f$ ) defines the number of memory locations required. The Feedforward RC controller includes the internal model as delays followed by a low-pass filter (LPF)  $Q(z)$ . This LPF increases the robustness of the system by reducing the high-frequency ripples in the processed signals. From Fig. 8, the transfer function of the RC controller is:

$$G_{FFRC}(z) = \frac{U_F(z)}{E(z)} = \frac{z^{-N} Q(z)}{1 - z^{-N}} \quad (31)$$

where  $N=f_s/f$ . The poles of  $G_{FFRC}(z)$  are located at  $2\pi jf$  where  $j = 0, 1, 2, \dots, J$  ( $J=N/2$ ). As shown from (31), the RC controller provides very high gain if the LPF gain is 1. Thus, the closed-loop system with the RC controller can eliminate the steady-state error and reject any arising disturbances. The error transfer function of the overall system can be found from:

$$\frac{E(z)}{I_g^*(z)} = \frac{k(1 + G_{PR}(z)G_{inv}(z))^{-1}(1 - z^{-N})}{1 - z^{-N} Q(z)(1 - kT(z))} \quad (32)$$

### C. INPUT CURRENT CONTROLLER

The input current controller is responsible for correcting the calculation errors from equation (13) due to parameters variations or external disturbances. Same as the PR transfer function in (25) and (26), the resonant controller is tuned at double the grid frequency are expressed as:

$$G_R(s) = \frac{k_r s}{s^2 + 4\omega^2} \quad (33a)$$

$$G_R(z) = \frac{0.5k_r t_s (1-z^{-2})}{1 + (\omega t_s)^2 + [(\omega t_s)^2 - 2]z^{-1} + [(\omega t_s)^2 + 1]z^{-2}} \quad (33b)$$

where  $k_r$  is the resonant gain of the controller.

### D. CONTROL SYSTEM DESIGN

The overall control system comprises of four gains ( $k$ ,  $k_p$ ,  $k_r$  and  $k_r$ ) and a LPF  $Q(z)$ . The gains and the LPF should be selected so that the roots of the system are always inside the unity circle. This can be ensured from the following steps:

a) The LPF can be expressed as:

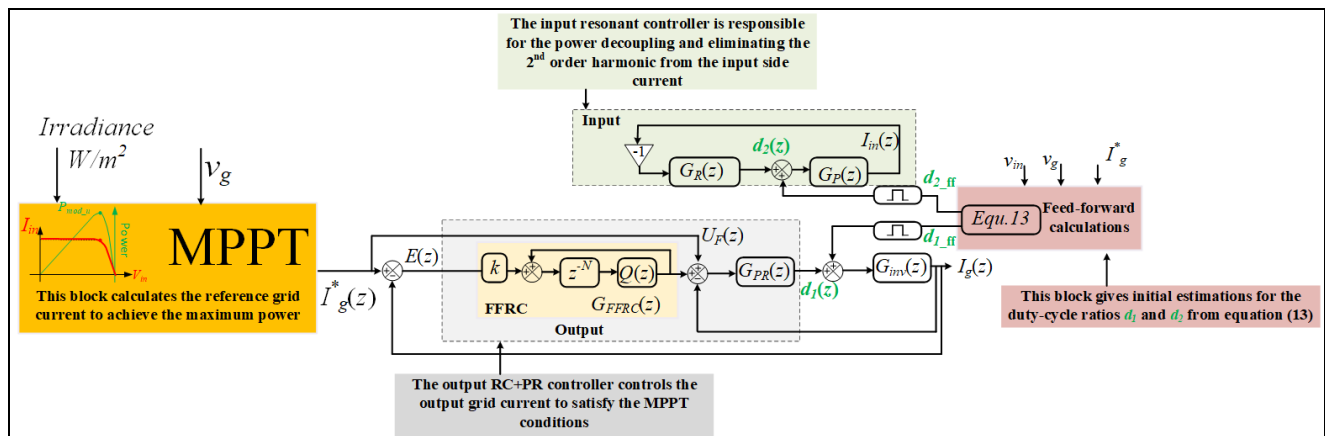


FIGURE 9. Block diagram of the proposed controller

$$Q(z) = \alpha_0 + \alpha_1 z^{-1} + \alpha_2 z^{-2} + \dots + \alpha_n z^{-n} \quad (34)$$

where  $n$  is the filter's order

The roots of the LPF are all inside the unity circle if the filter's gains are selected as :

$$\alpha_0 + \alpha_1 + \alpha_2 + \dots + \alpha_n = 1 \quad (35)$$

- b) To stabilise the closed-loop transfer function  $T(z)$ , the roots of  $(1-kT(z)) = 0$  should be kept inside the unit circle. This can be achieved by the careful choice of the gains  $k$ ,  $k_p$  and  $k_r$ . From the small-signal model in (27), the poles of the Cuk inverter transfer function  $G_{inv}(z)$  will move to the RHP with increasing the duty cycle ratios or the input voltage. Also, the values of the two zeros will become smaller. This means that the stability margins of the inverter will be inversely proportional with the invert's power. Thus, the controller gains should be designed at the maximum expected power for the inverter.
- c) The roots of  $1+G_R(z)G_{inv}(z) = 0$  are located inside the unit circle by adjusting the resonant controller's gain  $k_r$ . The eliminating time required until  $i_m(t)$  is constant (and the the 2<sup>nd</sup> order harmonic is removed) is not critical. Thus,  $k_r$  can be chosen freely only to keep  $G_R(z)G_{inv}(z)$  is stable without the necessity of the controller to be fast.

## VI. EXPERIMENTAL RESULTS

Fig. 10 shows the experimental prototype for the modular energy conversion system. The modules have changeable terminals to ease testing different inverter modules. The system is controlled by TMS32028335 DSP and has the same parameters in Table I to inject 1 kW into the grid. The nominal power of each module in this system is 250 W and the maximum allowed power is limited to 500 W and the maximum input voltage is 250V.

At these conditions, the worst-case transfer function for the Cuk inverter can be obtained from (29) as:

$$G_{inv}(z) = \frac{\tilde{i}_g(z)}{d_1(z)} = \frac{-0.01z^3 - 0.02z^2 + 0.05z + 0.04}{z^5 + 0.6z^4 + 0.45z^3 - 0.5z^2 + 0.25z - 0.15} \quad (36)$$

 TABLE I  
SYSTEM'S PARAMETERS

Symbol	Parameter	Value
$P_{mod}$	Module's power	250 W
$n$	Number of modules	4
$V_{in}$	Nominal input voltage	50 V
$V_g$	Grid voltage peak	324 V
$f$	Grid frequency	50 Hz
$f_s$	Switching (sampling) frequency	50 kHz
$L_f$	Grid transformer's inductance	0.1 mH
$H$	Transformer turns' ratio	1
$S_1-S_5$	Semiconductor switch	IRG4PC50FPbF 600V – 70A
$D_1-D_5$	Diode	FFSH40120ADN 1200V – 135A

The PR controller gains  $k_p$  and  $k_r$  are chosen as 1.5 and 1.8 respectively so the gain and phase margins of the closed loop transfer function  $T(z)$  in (28) are 30 dB and 80° respectively. Practically, three samples are sufficient for the LPF to perform the required filtering and hence it is chosen as  $Q(z) = 0.15z^2 + 0.15z^{-1} + 0.7$ . For the FFRC controller, the roots of  $1-kT(z)$  will be all inside the unit circle if the gain  $k = 1.5$ . The input's side resonant controller gain can be chosen independently as a small value where  $k_r = 0.2$ .

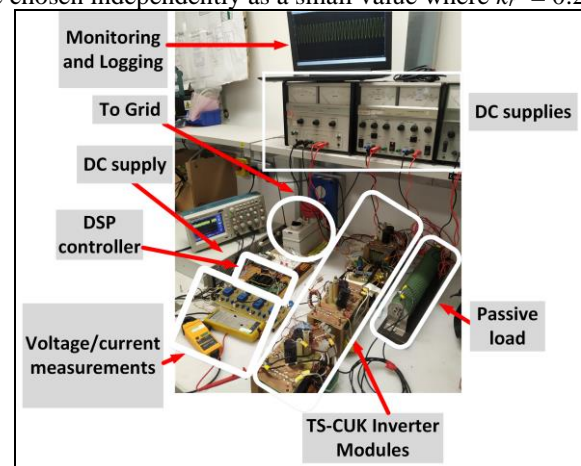


FIGURE 10. Experimental rig

The same steps have been taken to fine-tune the control

loops' gains for other three inverters Sepic, F5 and P5. Fig. 11 shows the operation of the system when operated by four Cuk-based modules in the normal condition. Fig 11a shows the input current of the four modules in the steady state where the 2<sup>nd</sup> order harmonic is eliminated in all modules. Fig. 11b shows the voltages across  $C_p$  and  $C_s$ . Fig. 11c shows the output voltages of the four modules. Fig. 11d shows the output current with the grid voltage.

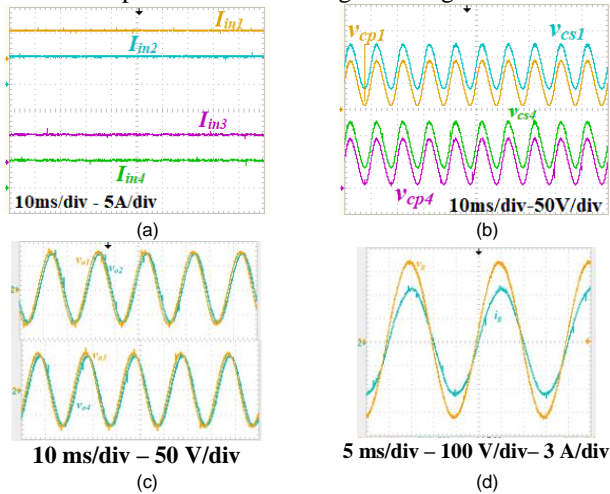


FIGURE 11. Experimental results of Cuk-based modular system: (a) input currents, (b) Capacitors voltages, (c) module's output voltages, and (d) grid voltage and current

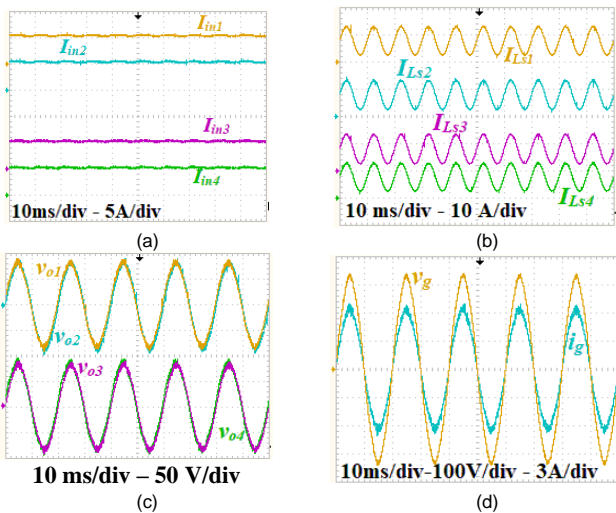


FIGURE 12. Experimental results of Sepic-based system: (a) input currents, (b)  $L_s$  currents, (c) output voltages, and (d) grid voltage/current

The same results for the system when operated by Sepic, F5 and P5-based modules are shown in Fig. 12, 13, and 14 respectively. In these normal conditions, the grid voltage is shared equally by the four modules. Fig. 15 shows the Fast Fourier Transform (FFT) for the four inverters' output currents.

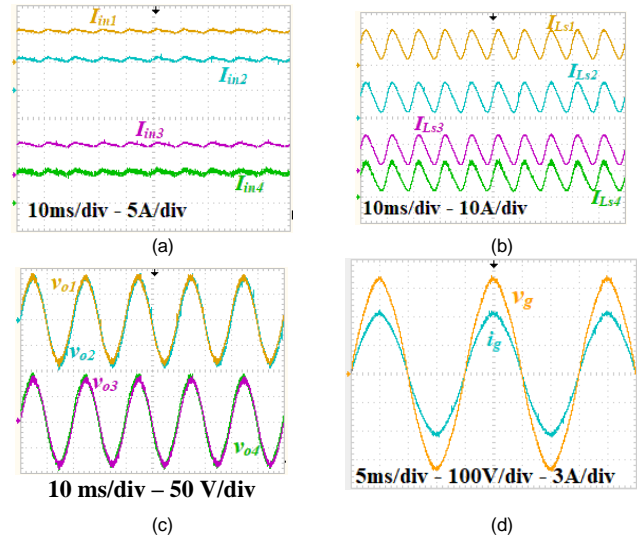


FIGURE 13. Experimental results of F5-based system: (a) input currents, (b)  $L_s$  currents, (c) output voltages, and (d) grid voltage/current

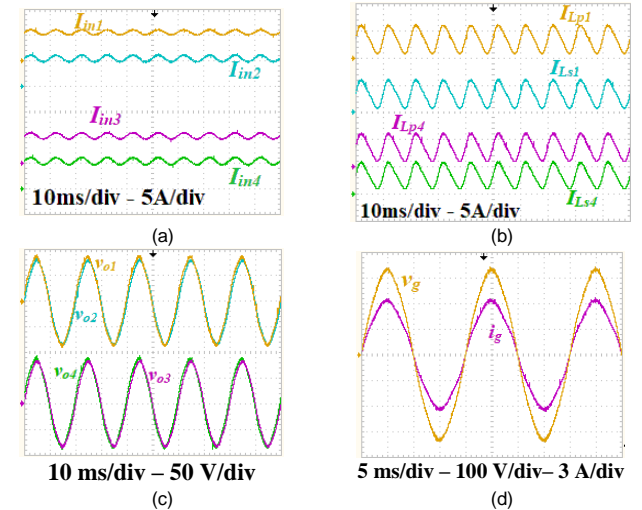


FIGURE 14. Experimental results of P5-based system: (a) input currents, (b)  $L_p / L_s$  currents, (c) output voltages, and (d) grid voltage/current

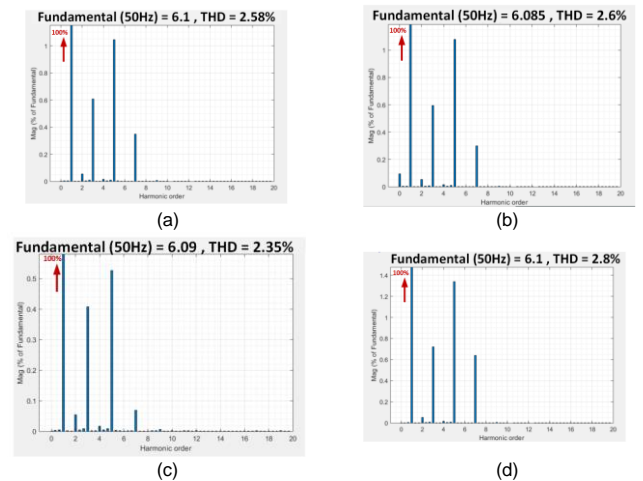


FIGURE 15. FFT of the inverters' output currents: (a) Cuk, (b) Sepic, (c) F5, and P5

Experimental case studies are carried out to mimic the performance of the system during partial shading conditions. At the shading time  $t_{sh}$ , the power of the 3<sup>rd</sup> and 4<sup>th</sup> Cuk-based modules drops to 20% while the 1<sup>st</sup> and 2<sup>nd</sup> modules' powers remain unchanged. Fig. 16a shows  $i_{in}$  and  $v_{in}$  for the 1<sup>st</sup> (unshaded) and the 4<sup>th</sup> (shaded) modules. Fig. 16b shows the output voltages  $v_{o1}$  and  $v_{o4}$  of the 1<sup>st</sup> and 4<sup>th</sup> modules where the controller changes the unshaded and shaded modules to keep their sum close to the grid voltage. The capacitors' voltages of the 1<sup>st</sup> and 4<sup>th</sup> modules are shown in Fig. 16c. Finally, the grid voltage with current is shown in Fig. 16d. In this case, the new reference current to the FFRC and PR controllers is calculated from (21) to extract 50W of the shaded modules while keeping the unshaded modules at 250W. As shown from Fig. 16b, the voltages  $v_o$  of unshaded modules increase while they decrease for the shaded modules as calculated from (21). The resultant power can be calculated as  $\approx 600$  W which is the maximum assumed power to be available from the input sources. Fig. 17 shows the I-V and power curves of the different shaded and unshaded modules at the steady-state conditions where the current controllers of all modules operate the system at the peaks of the power curves to extract the maximum available power during shading conditions. It should be noted that if more than one PV module are completely shaded, the unshaded modules will be required to generate higher output voltages to compensate for the difference and match the voltage to the grid. If the output voltages of the unshaded modules exceed the maximum allowed stress on the switches, the MPPT will not be achievable and the system output power will be restricted.

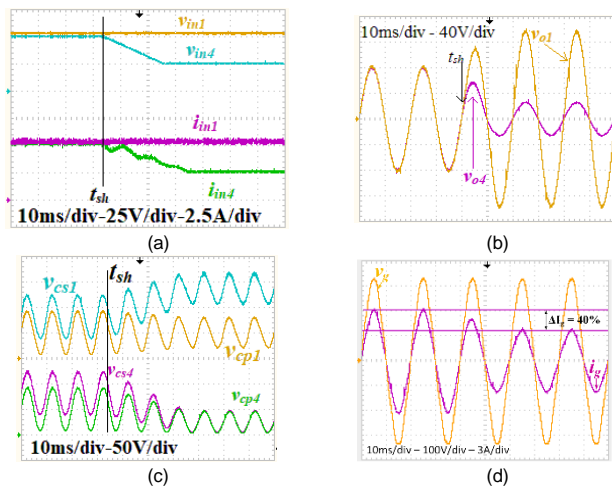


FIGURE 16. Partial shading conditions: (a) input voltages/currents, (b) module's output voltages, (c) capacitors voltages, and (d) grid voltage and current

## VII. PARAMETERS SELECTION AND COMPARISON

This section presents the steps for parameters selection process for different inverters and comparisons between the different candidates' modules in terms of their sizes, losses

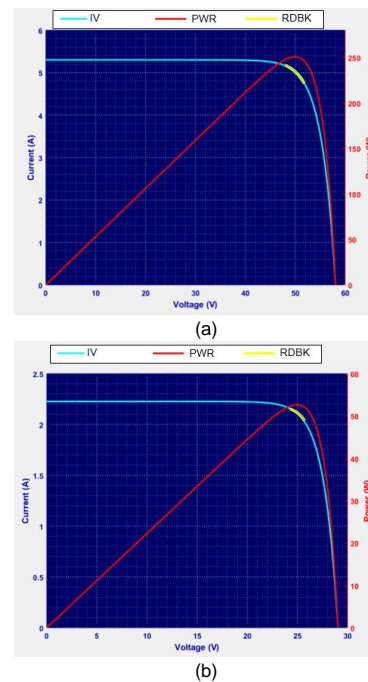


FIGURE 17. IV curves of the modules: (a) unshaded modules (1 and 2), (b) shaded modules (3 and 4)

and performances. All modules have the same semiconductor stresses but they have different current and voltage ripples and therefore the passive elements' values will vary in order to achieve the same operating conditions.

### A. PARAMETERS SELECTION

The detailed parameter selection process for switched mode power supplies has already been discussed in many publications [8]-[10] and [13]. This subsection will present a practical methods to select the passive elements and the transformer cores.

#### 1) PASSIVE ELEMENTS

For Cuk-based module as an example, the relation between input and output inductors and currents can be found from:

$$L_m = \frac{V_{in} \Delta t}{\Delta I_m} = \frac{D V_{in}}{f_s \Delta I_m} \quad (37)$$

If the maximum acceptable limit factor for the input and output currents' ripples are  $x_{Lin}$  and  $x_{Lo}$  respectively, so  $L_{in}$  and  $L_o$  can be expressed as:

$$x_{Lin} = \frac{\Delta I_{in(peak)}}{I_{in}} \text{ and } x_{Lo} = \frac{\Delta i_{o(peak)}}{i_g} \quad (38a)$$

$$L_{in} = \frac{D_{max} V_{in}}{f_s I_{in} x_{Lin}} \quad (38b)$$

$$L_o = \frac{(1 - D_{max}) V_o}{f_s i_g x_{Lo}} \quad (38c)$$

Substituting in equations (4) and (37), the modules' inductors should be chosen as:

$$L_m > \frac{nV_g V_{in}^2}{(V_g + nHV_{in})f_s P_{dc} x_{Lin}} \quad (39a)$$

$$L_o > \frac{V_{in} V_g^2 H \cos(\gamma)}{2f_s P_{dc} x_{Lin} (V_g + nHV_{in})} \quad (39b)$$

Similarly, the primary and secondary capacitors are expressed as:

$$C_p = \frac{I_m \Delta t}{\Delta V_{cp}} = \frac{I_m (1-D)}{f_s x_{cp} V_{cp}} \quad (40a)$$

$$C_s = \frac{I_m / H \Delta t}{\Delta V_{cs}} = \frac{I_m (1-D)}{H f_s x_{cs} V_{cs}} \quad (40b)$$

where  $x_{cp}$  and  $x_{cs}$  are the maximum acceptable voltage ripple factor for the capacitors' voltages as:

$$x_{cp} = \frac{\Delta v_{c_p(peak)}}{V_{cp}} \quad \text{and} \quad x_{cs} = \frac{\Delta v_{c_s(peak)}}{V_{cs}} \quad (41)$$

Similarly, the Cuk module's capacitors are chosen as:

$$C_p > \frac{P_{dc} H (1+H)}{f_s x_{Cp} (V_g + nHV_{in}) (V_{cdc} + V_{cm})} \quad (42a)$$

$$C_s > \frac{P_{dc} (1+H)}{f_s x_{Cs} (V_g + nHV_{in}) (V_{cdc} + V_{cm})} \quad (42b)$$

Finally, the output current THD is further reduced by the aid of the output capacitor  $C_o$ . The output capacitor is selected as:

$$C_o = \frac{I_g}{2\pi V_g f_s x_o} \quad \text{where} \quad x_o = \frac{\Delta i_{g(peak)}}{\Delta i_{o(peak)}} \quad (43)$$

In the same way, the passive elements of the different modules can be deduced and listed in Table 2. II. In practice, the values of these passive elements are chosen to keep the voltage and current limits below 10% while the THD of the output current should be kept below 5% to meet grid standards.

## 2) TRANSFORMERS' DESIGN

It is required to minimise the volume, size and weight of the transformer core in the different inverter topologies. Nanocrystalline ribbon materials can reduce the transformer cores' size significantly due to its high magnetic permeability which exceeds 30,000 H/m [21]. The first step is to calculate the rms voltage across the transformer terminals. The rms voltages at the rated power are listed in Table III. Then, the specified magnetizing inductance is calculated from [22]:

$$L_m^* = \frac{V_{rms}}{2\pi f_s I_{rms}} k_{Lm} \quad (44)$$

It is required to satisfy this magnetizing inductance while keeping the flux density below its maximum value. The constant  $k_{Lm}$  depends on the type of the converter and is subjected for fine tuning. Then, the magnetising inductance  $L_m$  is calculated from [22] as:

$$L_m = \frac{N^2 A_c \mu_o \mu_r S_F}{l_c} \quad (45)$$

Where  $N$  is the number of turns,  $\mu_o$  and  $\mu_r$  are the permeabilities of the air and the core's materials,  $l_c$  is the

TABLE II  
FORMULAS FOR PARAMETERS SELECTION

Module	Element	Formula >	Ripple factor
F5	$C_{in}$	$\frac{V_g I_g H}{(V_g + nHV_{in}) f_s P_{dc} x_{Lin}}$	$x_{cin} = \frac{\Delta V_{cin(peak)}}{V_{in}}$
	$L_{in}$	$\frac{nV_g V_{in}^2}{(V_g + nHV_{in}) f_s P_{dc} x_{Lin}}$	$x_{Lin} = \frac{\Delta I_{in(peak)}}{I_{in}}$
	$L_s$	$\frac{V_g V_{in} H}{(V_g + n^2 HV_{in}) f_s I_m x_{Ls}}$	$x_{Ls} = \frac{\Delta I_{Ls(peak)}}{I_g}$
	$C_o$	$\frac{2P_{dc}}{H f_s V_{in} x_o \cos(\gamma) (V_g + n^2 HV_{in})}$	$x_o = \frac{\Delta I_g(peak)}{I_g}$
Sepic	$L_{in}$	$\frac{nV_g V_{in}^2}{(V_g + nHV_{in}) f_s P_{dc} x_{Lin}}$	$x_{Lin} = \frac{\Delta I_{in(peak)}}{I_{in}}$
	$C_p$	$\frac{P_{dc} H}{V_{in} f_s x_{Cp} (V_g + nHV_{in})}$	$x_{cp} = \frac{\Delta V_{c_p(peak)}}{V_{in}}$
	$C_s$	$\frac{P_{dc}}{V_{in} f_s x_{Cs} H^2 (V_g + nHV_{in})}$	$x_{cs} = \frac{\Delta V_{c_s(peak)}}{HV_{in}}$
	$L_s$	$\frac{V_g V_{in} H}{(V_g + n^2 HV_{in}) f_s I_m x_{Ls}}$	$x_{L2} = \frac{\Delta I_{Ls(peak)}}{I_{Ls}}$
	$C_o$	$\frac{2P_{dc}}{H f_s V_{in} x_o \cos(\gamma) (V_g + n^2 HV_{in})}$	$x_o = \frac{\Delta I_g(peak)}{I_g}$
P5	$L_{in}, C_{in}, C_o$	Same as F5	Same as F5
	$L_p$	$\frac{V_g V_{in}}{H (V_g + n^2 HV_{in}) f_s I_m x_{Ls}}$	$x_{Lp} = \frac{\Delta I_{Lp(peak)}}{I_g}$
	$C_p$	$\frac{P_{dc} H}{V_{in} f_s x_{Cp} (V_g + nHV_{in})}$	$x_{cp} = \frac{\Delta V_{c_p(peak)}}{V_{in}}$
	$L_s$	$\frac{V_g V_{in} H}{(V_g + n^2 HV_{in}) f_s I_m x_{Ls}}$	$x_{Ls} = \frac{\Delta I_{Ls(peak)}}{I_{Ls}}$
	$C_s$	$\frac{P_{dc}}{V_{in} f_s x_{Cs} H^2 (V_g + nHV_{in})}$	$x_{cs} = \frac{\Delta V_{c_s(peak)}}{V_{cs}}$

TABLE III  
TRANSFORMER'S PARAMETERS

	Cuk	Sepic	F5	P5
$V_{rms}$ (V)	$\approx 35.355$	$\approx 35.355$	$\approx 70$	$\approx 25$
$L_m^*$ ( $\mu$ H)	80	67	178	47
N	15	13	20	10
$L_m$ ( $\mu$ H)	160	150	340	90
$B_{opt}$ (T)	0.7	0.75	1.1	0.6
$B_{sat}$ (T)	1.5	1.5	2	1.5

mean length of the magnetic path,  $A_c$  is the cross section area of the cores and  $S_F$  is the number of cores needed to achieve the required area product  $A_p$ . The values of  $A_c$  and  $l_c$  are obtained from the datasheet of the core and  $A_p$  is calculated from [23]:

$$A_p = \frac{4\sqrt{2} \times VA}{B_{opt} f_s} \quad (46a)$$

$$B_{opt} = \frac{1.3 \times 10^4}{VA \times f_s^{1/2}} \quad (46b)$$

Finally, it is required to confirm that the transformer flux density will be below the saturation limits  $B_{sat}$  of the core as:

$$B_{opt} \leq B_{sat} \quad (47)$$

The resultant values of this process are listed in Table III and have been used to design the transformer cores.

### B. PERFORMANCE EVALUATION

In order to evaluate the performances of the different modules, the proposed system has been tested in the normal operation with the four single-phase inverter modules.

TABLE IV  
PASSIVE ELEMENTS' VALUES OF THE OPERATED SYSTEM

Module	Element	Formula >	Ripple factor at $P_{mod}$
Cuk	$L_{in}$	3 mH, 0.1Ω	5%
	$L_o$	2 mH, 0.067 Ω	5%
	$C_p$ & $C_s$	75 μF	1%
	$C_o$	6 μF	1%
Sepic	$L_{in}$	3 mH, 0.1Ω	5%
	$C_p$ & $C_s$	10 μF	6%
	$L_s$	10 mH, 0.3 Ω	<1%
	$C_o$	50 μF	1%
F5	$L_{in}$	0.5 mH, $1 \times 10^{-3}$ Ω	5%
	$C_{in}$	1 μF	<10%
	$L_s$	10 mH, 0.3 Ω	<1%
	$C_o$	50 μF	1%
P5	$L_{in}$	0.5 mH, $1 \times 10^{-3}$ Ω	5%
	$C_{in}$	1 μF	<10%
	$C_o$	50 μF	1%
	$C_p$ & $C_s$	10 μF	6%
	$L_p$	3 mH, 0.1 Ω	<1%
	$L_s$	6 mH, 0.2 Ω	<1%

#### 1) PASSIVE ELEMENTS AND EFFICIENCIES

The passive elements of each module have been selected to keep the high-frequency current and voltage ripples = 5% of the nominal current and voltage values at the rated power. These passive elements of the different elements are calculated from Table II and listed in Table IV. Therefore, the THD of the output currents should be close and less than 5% for all inverters. Although the high-frequency ripples in the output currents are the same for all inverters as shown in the experiments, the slight differences in the THD of the output currents in Fig. 15 occur due to the low order 3<sup>rd</sup>, 5<sup>th</sup>, and 7<sup>th</sup> because they have different transfer functions and therefore different poles locations. These low order harmonics will increase if the passive elements in the inverters are increased in case of reducing the switching frequency. In Fig. 15, it has been shown that the THD of the output currents is always less than 5% as pre-calculated from Table IV. However, if the low order harmonics increased and lead the THD to exceed 5%, harmonic eliminators can be used in the control scheme to remove these components as shown in [1], but this will add to the complexity of the control system. For energy storage elements such as  $C_p$ ,  $C_s$  in Cuk-module or  $L_s$  and  $L_p$  in other modules, the values are chosen to ensure that the element will withstand the peak value and to avoid saturation. Fig. 18 shows a comparison between the sizes of different modules. A comparison

between the efficiencies of the different module inverters (from Fig. 3) is conducted using MATLAB/SIMULINK and plotted in Fig. 19. Cuk-based module requires bigger capacitor to store the oscillating energy while all other components are relatively small. As shown in the efficiency comparison in Fig. 19, this module has the best efficiency performance as it experiences the least equivalent Series Resistance (ESR) and transformer core losses. For Sepic-based module, the ESR losses increases as the energy is stored in  $L_s$  which has relatively higher parasitic resistance when compared with the capacitors leads and therefore the total efficiency decreased. As the transformer core transfers the energy instantaneously between the primary and secondary sides, small cores can be used for isolation in case of Cuk, Sepic, and P5. F5-based modules have the worst efficiency when compared with the other candidates, this comes from the fact that bigger transformer magnetic core should be used as it stores the energy temporarily and then releases this energy after period of time. P5-based modules employ the smallest capacitors as the average voltages across  $C_p$  and  $C_s$  are always zero.

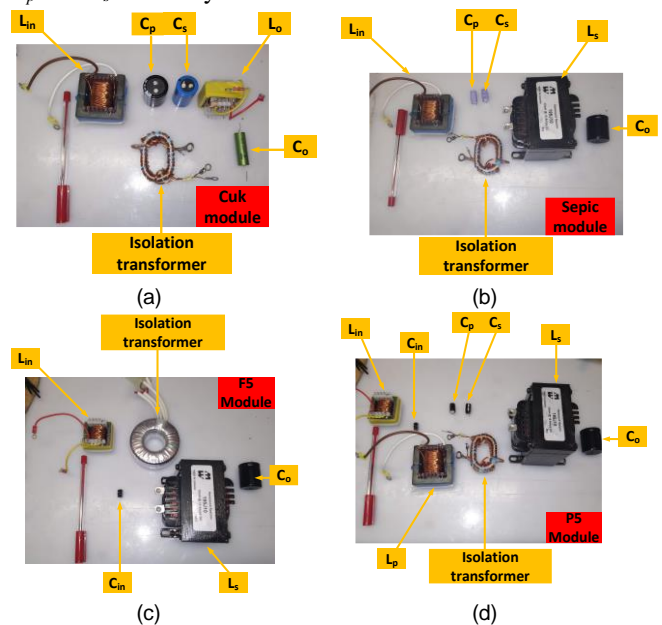


FIGURE 18. Passive elements breakdown: (a) Cuk, (b) Sepic, (c) F5 and (d) P5

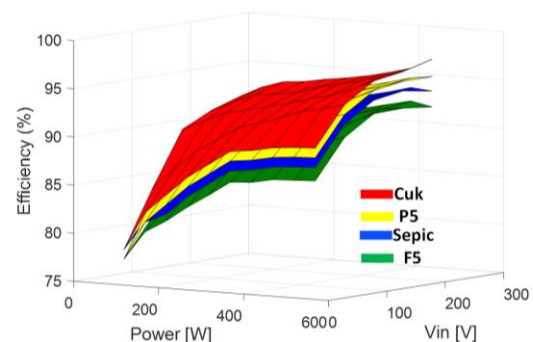


FIGURE 19. Simulated efficiencies of different inverters configurations

The ESR losses are lower than F5 and Sepic-based modules losses as the oscillating energy is stored in the two inductors ( $L_p$  &  $L_s$ ). It should be mentioned that although Sepic, F5, P5-based modules have lower efficiency and bigger sizes than the Cuk-based module, they have the advantage of using smaller capacitors which may be an important feature for improving the total system's reliability especially when fewer modules are employed with high boosting ratio  $V_o/V_{in}$ . With fewer modules and higher boosting ratios, higher voltage stresses are generated across the capacitors which may reduce the system's reliability in these conditions. Fig. 20a shows the practical efficiencies of the inverter modules at  $V_{in} = 50V$ .

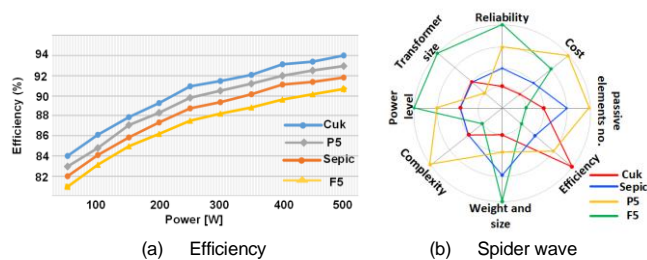


FIGURE 20. Comparative analysis of different inverter modules

A comparison between the efficiencies of the different Cuk inverters configuration (from Fig. 4) is plotted in Fig. 21. The comparison is conducted using the same passive elements and devices in Table I. The efficiency of the proposed Cuk inverter is close to the differential-Cuk when  $V_{in}$  is low. The proposed Cuk inverter is superior to other Cuk configurations when the output power increase because the reduced losses in its input inductor. It should be noted that these efficiencies are calculated considering the inverters' power losses with respect to the input electrical power from the dc source. However, when the other Cuk configurations are connected to PV panels, the 2<sup>nd</sup> order harmonic component in the input current, inevitably, will lead to power oscillation between points 3 and 4 in Fig. 1a. This will reduce the extracted PV power below its maximum available point and hence will reduce the effective efficiency.

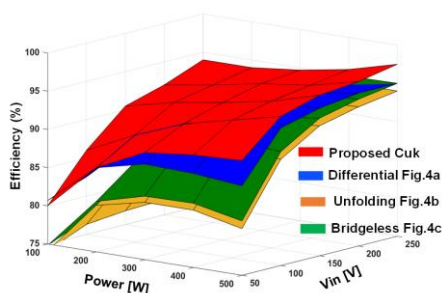


FIGURE 21. Simulated efficiencies of Cuk inverters configurations

## 2) DYNAMIC PERFORMANCES COMPARISON

This subsection discusses the dynamic responses of the different inverter topologies during grid instability

conditions. Table V shows the controller gains' values in order to achieve 30 dB and 80° stability margins for all inverters. The Cuk inverter Transfer Function is fourth-order and the control system can reach bandwidth of  $\approx 1.8$  kHz. This can be increased if the optional capacitor  $C_o$  is reduced or removed. Sepic inverter requires higher values of  $C_o$  and  $L_s$  when compared with the Cuk inverter and therefore the bandwidth is lower. F5 has the highest bandwidth as it needs lower total capacitances and inductances. P5 has the highest order among all inverters and therefore the control design process is restricted. Fig. 22 shows the response of the four inverters when the grid voltage dropped to 20% of its nominal value to mimic a phase-to-ground fault. Because F5 inverter has the highest bandwidth in its control system, the current controller recovered the current in less than half-cycle to enable the grid protection devices to operate without destroying the inverter's switches.

TABLE V  
CONTROLLER GAINS' VALUES

Module	gain	value	Bandwidth	Inverter Order
Cuk	$k_p$ and $k_r$	0.15, 0.5	$\approx 1.8$ kHz	4 (or 3 if $C_o$ is removed)
	$k$	1.5		
	$k_r^*$	0.5		
Sepic	$k_p$ and $k_r$	0.1, 0.4	$\approx 1.2$ kHz	4
	$k$	1.5		
	$k_r^*$	0.5		
F5	$k_p$ and $k_r$	0.2, 1	$\approx 1.9$ kHz	4
	$k$	1.5		
	$k_r^*$	0.5		
P5	$k_p$ and $k_r$	0.07, 0.1	$\approx 600$ Hz	5

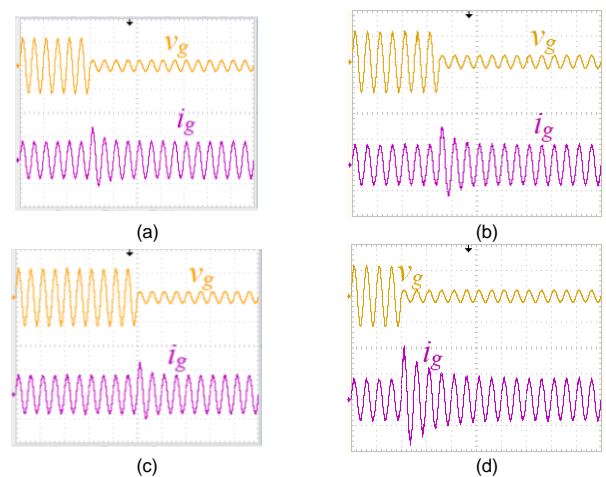


FIGURE 22. Dynamic response of the four inverters: (a) Cuk, (b) Sepic, (c) F5 and (d) P5.

P5 shows the worst performance as it takes more than one cycle to recover the current after the fault. This comes from the fact that P5 stems from a fifth-order converter and therefore it is difficult to increase the controller bandwidth with a single loop controller. A solution to this issue has been proposed in [24] where an additional loop can increase the controller bandwidth and hence its speed. Cuk and

Sepic inverters' speed to recover the grid currents are between F5 and P5.

### 3) OVERALL EVALUATION

Following to the previous analyses and results, important findings and recommendations can be made as:

- The efficiency of the Cuk inverter in Fig. 3a is the highest and therefore it is favoured to maximise the harvested power from the system. However, as the oscillating energy is stored in the capacitors  $C_p$  and  $C_s$ , the reliability may be reduced when the operating voltage increases, or the number of modules is reduced and the Cuk inverter will not be suitable in this case as the voltage stresses across the capacitors will be high.
- The F5 inverter has the highest losses, lowest efficiency, and the biggest transformer size.
- From the control point of view, the transfer function of F5 inverter enables for achieving high bandwidth and hence the control design is less complex. This affects the dynamic response during faults and instabilities. On the other hand, the P5 inverter's transfer function is of the highest order and therefore the control design is more difficult. In this context, the F5 inverter is preferred when the switching frequency is low (<5kHz) and large passive elements are employed to reduce the current and voltage ripples.
- Despite of the abovementioned drawbacks, P5 inverter's capacitors have zero average voltages and therefore small capacitors can be used. This increases the reliability of the inverter and reduces the size of the transformer. Therefore, the P5 inverter is favoured if the switching frequency can be increased (>50kHz).
- In general, the efficiencies of the Sepic, F5, and P5 inverters are lower than the Cuk inverter as they store the oscillating energy inside the shunt inductors  $L_s$ . For this reason, the ESR of  $L_s$  affects the power losses significantly.
- The Sepic inverter shows a good trade-off between the size, efficiency, complexity of the control design, and reliability if moderate module number, voltage level, and switching frequency have been used.

### VIII. CONCLUSION

The paper presents a modular energy conversion structure for grid-connected PV system based on four single-phase buck-boost isolated current source inverters. The four modules have been investigated in terms of power losses, size, performance and voltage/current ripples. The proposed system is capable of controlling the output active and reactive power injected to the grid while operating the PV panels at the maximum power points. The MPPT operation is achieved by storing the oscillating power component in storage elements inside the inverters. The modular system offers modularity, scalability and improve the reliability by reducing the voltage and current stresses across each

module's passive elements as well as providing redundant modules in case of module's failure. Moreover, the modular structure can operate during partial shading conditions if the individual modules' currents and voltages are measured.

### ACKNOWLEDGMENT

We would like to acknowledge the support received from Shaqra University.

### REFERENCES

- [1] M. Mirjafari, S. Harb and R. S. Balog, "Multiobjective Optimization and Topology Selection for a Module-Integrated Inverter," in *IEEE Transactions on Power Electronics*, vol. 30, no. 8, pp. 4219-4231, Aug. 2015
- [2] S. B. Kjaer, J. K. Pederson, and F. Blaabjerg, "A review of single-phase grid-connected inverters for photovoltaic modules," *IEEE Trans. Ind. Appl.*, vol. 41, no. 5, pp. 1292-1306, Sep/Oct. 2005.
- [3] S. B. Kjaer, J. K. Pedersen, and F. Blaabjerg, "Power inverter topologies for photovoltaic modules—A review," in *Proc. IEEE IAS Conf.*, 2002, pp. 782-788.
- [4] Q. Li and P. Wolfs, "A review of the single phase photovoltaic module integrated converter topologies with three different DC link configurations," *IEEE Trans. Power Electron.*, vol. 23, no. 3, pp. 1320-1333, May. 2008
- [5] D. Leuenberger and J. Biela, "PV-Module-Integrated AC Inverters (AC Modules) With Subpanel MPP Tracking," in *IEEE Transactions on Power Electronics*, vol. 32, no. 8, pp. 6105-6118, Aug. 2017.
- [6] T. Shimizu, K. Wada, and N. Nakamura, "Flyback-type single-phase utility interactive inverter with power pulsation decoupling on the DC input for an AC photovoltaic module system," *IEEE Trans. Power Electron.*, vol. 21, no. 5, pp. 1264-1272, Sep. 2006.
- [7] L. Zhang, K. Sun, Y. W. Li, Xi. Lu, and J. Zhao "A Distributed Power Control of Series-connected Module Integrated Inverters for PV Grid-tied Applications," *IEEE Trans. Power Electron.*, vol. 33, no. 19, pp. 7698 - 7707, Sep. 2018
- [8] A. Darwish, A. M. Massoud, D. Holliday, S. Ahmed and B. W. Williams, "Single-Stage three-phase differential-mode buck-boost inverters with continuous input current for PV Applications," in *IEEE Transactions on Power Electronics*, vol. 31, no. 12, pp. 8218-8236, Dec. 2016.
- [9] A. Darwish Badawy, "Current source dc-dc and dc-ac converters with continuous energy flow," Degree of Doctor of Philosophy, Department of Electronics and Electrical Engineering, University of Strathclyde, Glasgow, 2015.
- [10] B. W. Williams, "Generation and analysis of canonical switching Cell DC to-DC converters," *IEEE Trans. Ind. Electron.*, vol. 61, no. 1, pp. 329-346, Jan. 2013.
- [11] M. R. Islam, Y. G. Guo, and J. G. Zhu, "A high-frequency link multilevel cascaded medium-voltage converter for direct grid integration of renewable energy systems," *IEEE Trans. Power Electron.*, vol. 29, no. 8, pp. 4167-4182, Aug. 2014.
- [12] A. Darwish, A. Elserougi, A. Abdel-Khalik, S. Ahmed, A. Massoud, D. Holliday, and B. Williams, "A single-stage three-phase DC/AC inverter based on Cuk converter for PV application," in *GCC Conference and Exhibition (GCC)*, 2013 7th IEEE, 2013, pp. 384-389
- [13] A. Darwish and M. A. Elgenedy, "Current-Source Modular Medium-Voltage Grid-Connected System With High-Frequency Isolation for Photovoltaic Applications," in *IEEE Transactions on Energy Conversion*, vol. 34, no. 1, pp. 255-266, March 2019.
- [14] S. Mehrnami and S. K. Mazumder, "Discontinuous modulation scheme for a differential-mode Cuk Inverter," *IEEE Trans. on Power Electron.*, vol. 30, no. 3, pp. 1242-1254, Mar. 2015
- [15] B. Han, J. Lee, M. Kim, "Repetitive controller with phaselead compensation for Cuk CCM inverter," *IEEE Trans. Ind. Electron.*, vol. 65, no. 3, pp. 2356-2367, Mar. 2018.

- [16] B. Han, J. Lai and M. Kim, "Bridgeless Cuk-Derived Single Power Conversion Inverter with Reactive Power Capability," in IEEE Transactions on Power Electronics. Early Access 2019.
- [17] A. Darwish, A. Massoud, D. Holliday, S. Ahmed and B. Williams, "Generation, performance evaluation and control design of single-phase differential-mode buck-boost current-source inverters," in IET Renewable Power Generation, vol. 10, no. 7, pp. 916-927, 7 2016.
- [18] N. Rabia "Advanced repetitive control of grid converters for power quality improvement" PhD Dissertation, University of Canterbury, 2015
- [19] Z. Zou, K. Zhou, Z. Wang and M. Cheng, "Frequency-Adaptive Fractional-Order Repetitive Control of Shunt Active Power Filters," in IEEE Transactions on Industrial Electronics, vol. 62, no. 3, pp. 1659-1668, March 2015.
- [20] B. A. Francis and W. M. Wonham. The internal model principle for linear multivariable regulators. Appl. Math. Optim., 1975
- [21] R. Burdt et al., "Evaluation of Nanocrystalline Materials, Amorphous Alloys and Ferrites for Repetitive-Magnetic Pulse Compression Applications," 2005 IEEE Pulsed Power Conference, Monterey, CA, 2005, pp. 843-847.
- [22] Y. Du, S. Baek, S. Bhattacharya and A. Q. Huang, "High-voltage high-frequency transformer design for a 7.2kV to 120V/240V 20kVA solid state transformer," IECON 2010 - 36th Annual Conference on IEEE Industrial Electronics Society, Glendale, AZ, 2010, pp. 493-498.
- [23] O. Aldosari, L. A. Garcia Rodriguez, J. C. Balda and S. K. Mazumder, "Design Trade-Offs for Medium- and High-Frequency Transformers for Isolated Power Converters in Distribution System Applications," 2018 9th IEEE International Symposium on Power Electronics for Distributed Generation Systems (PEDG), Charlotte, NC, 2018, pp. 1-7.
- [24] A. Darwish, AS. Abdel-Khalik, A. Elserougi, S. Ahmed, A. Massoud, "Fault current contribution scenarios for grid-connected voltage source inverter-based distributed generation with an LCL filter". Electr Power Syst Res 2013;104:93-103



**Ahmed Darwish** received the B.Sc. and M.Sc. degrees in electrical engineering from the Faculty of Engineering, Alexandria University, Egypt, in 2008 and 2012, respectively, and the Ph.D degree in electrical engineering from Electric and Electronic Engineering Department at the University of Strathclyde, Glasgow, U.K., in 2016.

From 2009 to 2012, he was a Research Assistant at Texas A&M University at Qatar. From 2015, he was a Postdoctoral Research Associate with PEDEC group at the University of Strathclyde for two years. He has joined Lancaster University as a Lecturer in Electrical Engineering in 2017. His research interests include dc-dc converters, multi-level converters, electric machines, digital control of power electronic systems, energy conversion, renewable energy, and power quality.



**Saud Alotaibi** received the B.Sc. degree in electrical engineering from Taif University, Taif, Saudi Arabia, in 2012, and the M.Sc. degree in electrical engineering from University of Nottingham, Nottingham, U.K, in 2016. Since 2013, he has been with College of Engineering, Shaqra University, where he is holding a lecturer position.

He is currently working toward his Ph.D. degree at the Department of Engineering, Lancaster University, Lancaster, U.K. His area of interest includes power electronics, dc-dc converters, multilevel converters, energy conversion, and power quality.



**Mohamed A. Elgenedy (SM'19)** received the B.Sc. (with first-class honors) and M.Sc. degrees in Electrical Engineering from Alexandria University, Egypt in 2007 and 2010, respectively, and the Ph.D. degree in Electrical and Electronic Engineering from the University of Strathclyde, Glasgow, U.K., in 2018. He is currently a

Postdoctoral Research Associate with PEDEC group at Strathclyde University, Glasgow, U.K. He is also an assistant lecturer with the Electrical Engineering Department, Faculty of Engineering, Alexandria University. From 2011 to 2013, he was with Spiretronic LLC, Houston, TX, USA, as a Research Engineer. From 2013 to 2014, he was a Research Associate at Texas A&M University at Qatar, Doha, Qatar. His research interests include high power electronics, pulse power generator, electric machine drives, energy conversion, electric vehicles and renewable energy.